Electronic Supplementary Material (ESI) for Nanoscale.

Supplementary Information: Graphene-porphyrin single-molecule transistors

Jan A. Mol,[1] Chit Siong Lau,[1] Wilfred J.M. Lewis,[2] Hatef Sadeghi,[3] Cecile Roche,[2] Arjen Cnossen,[2] Jamie H. Warner,[1] Colin J. Lambert,[3] Harry L. Anderson,[2] and G. Andrew D. Briggs[1]

[1]*Department of Materials, University of Oxford, 16 Parks Road, Oxford OX1 3PH, UK*
[2]*Department of Chemistry, University of Oxford, Chemistry Research Laboratory, Mansfield Road, Oxford OX1 3TA, UK*
[3]*Quantum Technology Centre, Physics Department, Lancaster University, LA1 4YB Lancaster, UK*

(Dated: June 22, 2015)

CONTENTS

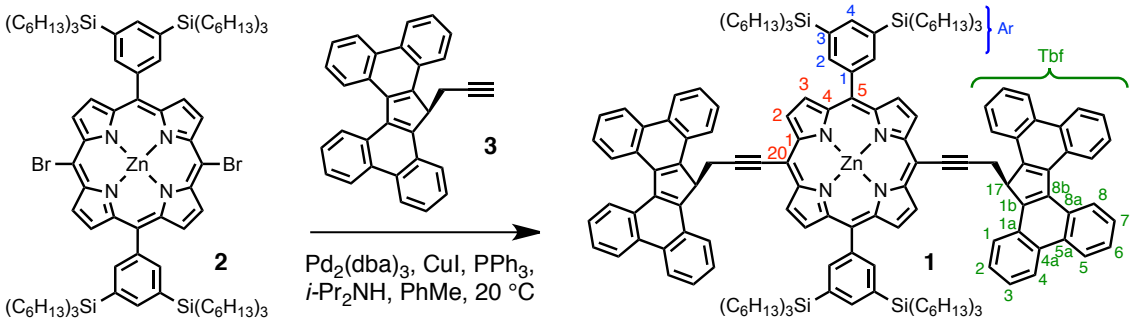

FIG. SI1: Synthesis of the bistetrabenzofluorene-porphyrin 1.

I. EXPERIMENTAL DETAILS

A. General Synthesis and Characterisation

Dibromoporphyrin **2**[1] and alkyne **3**[2,3] were synthesised following reported procedures. Other reagents were purchased from commercial sources. Solvents were used as supplied (analytical/HPLC-grade from Fisher or Sigma-Aldrich) or dried by passing through alumina with N_2. Diisopropylamine (DIPA) was distilled from CaH_2 under Ar. Eluent mixtures are reported in volume/volume %. Column chromatography was carried out using Merck Geduran silicagel 60 under N_2 pressure. TLC was carried out on Merck silica gel 60 F254 Al plates. MALDI-MS was carried out in positive reflectron mode using a Waters MALDI-micro X instrument using dithranol as a matrix. NMR measurements were recorded using a Bruker AVII400 or AVII500 instrument. All peaks were referenced to the residual solvent peak and spectra were analysed using Bruker TopSpinTM 3.1 software. UV-vis spectra were recorded using a PerkinElmer Lambda 25 instrument.

B. Molecular Synthesis

The synthesis of the porphyrin-based molecular wire with tetrabenzo[a,c,g,i]fluorene end-groups (**1**) was achieved by palladium-catalyzed Sonogashira cross-coupling of dibromoporphyrin **2**[1] with alkyne **3**[2,3], as shown in Figure 1. Dibromoporphyrin **2** (300 mg, 167 μmol), alkyne **3** (167 mg, 417 μmol) and PPh_3 (17.3 mg, 66 μmol) were dissolved in toluene (7.5 mL) and DIPA (7.5 mL). The mixture was then degassed via five freeze-pump-thaw cycles, $Pd_2(dba)_3$ (9.5 mg, 17 μmol) and CuI (6.3 mg, 33 μmol) added and stirred in the dark at 20 °C under an atmosphere of argon for 48 h. The mixture was then evaporated and dried under vacuum in the dark before being purified by column chromatography on silica gel (10% toluene, 1% pyridine in petroleum ether) to yield compound **1** as a dark green solid (172 mg, 42%). The molecule (without anchor groups) used for the control experiments is shown in Figure 2.

C. Chemical Data

^{1}H NMR (400 MHz, $CDCl_3$): δ_H 8.88 (d, 4H, $CH_{\text{Tbf-4}}$), 8.86 (d, 4H, $CH_{\text{Porph-2}}$), 8.83 (d, 4H, $CH_{\text{Tbf-5}}$), 8.76 (d, 4H, $CH_{\text{Tbf-1}}$), 8.60 (d, 4H, $CH_{\text{Tbf-8}}$), 8.47 (d, 4H, $CH_{\text{Porph-3}}$), 8.19 (s, 4H, $CH_{\text{Ar-2}}$), 8.11 (s, 2H, $CH_{\text{Ar-4}}$) , 7.82 (t, 4H, $CH_{\text{Tbf-2}}$), 7.74 (t, 4H, $CH_{\text{Tbf-3}}$), 7.59 (t, 4H, $CH_{\text{Tbf-6}}$), 7.37 (t, 4H, $CH_{\text{Tbf-7}}$), 5.45 (t, 2H, $CH_{\text{Tbf-17}}$), 4.15 (d, 4H, CCCH_2), 1.63 (m, 24H, $SiCH_2CH_2$), 1.51 (m, 24H, $SiCH_2CH_2CH_2$), 1.40 (m, 48H, $SiCH_2CH_2CH_2CH_2CH_2CH_3$), 1.07 (m, 24H, $SiCH_2$), 0.93 ppm (t, 36H, CH_3). ^{13}C NMR (500 MHz, $CDCl_3$): δ_C 151.8 (Porph-1), 149.9 (Porph-4), 144.1 (Tbf-1b), 141.2 (Tbf-1a), 140.5 (Ar-2) 138.9 (Ar-4), 137.4 (Tbf-8b), 134.5 (Ar-3), 132.1 (Tbf-4a), 132.0 (Porph-2), 131.0 (Porph-5), 130.5 (Porph-3), 128.8 (Tbf-8a), 128.4 (Tbf-5a), 127.8 (Tbf-8), 127.3 (Tbf-2), 126.2 (Tbf-3), 125.9 (Tbf-6), 125.0 (Tbf-7), 124.9 (Tbf-1), 123.7 (Tbf-4), 123.6 (Tbf-4), 122.7 (Ar-1), 100.9 (Porph-20), 93.0 ($CCCH_2CH$), 86.6 ($CCCH_2CH$), 47.3 (Tbf-17), 33.7 ($SiCH_2CH_2CH_2CH_2CH_2CH_3$), 31.7 ($SiCH_2CH_2CH_2CH_2CH_2CH_3$), 26.7 ($CCCH_2CH$), 24.3 ($SiCH_2CH_2CH_2CH_2CH_2CH_3$), 22.9 ($SiCH_2CH_2CH_2CH_2CH_2CH_3$), 14.2 ($SiCH_2CH_2CH_2CH_2CH_2CH_3$), 12.9 ppm ($SiCH_2CH_2CH_2CH_2-CH_2CH_3$).
MALDI-TOF: m/z 2456.6-2464.5 $C_{168}H_{208}N_4Si_4Zn$ requires 2460.48. UV-VIS: λ_{max} 439 nm, log (ϵ/dm^3 cm^{-1} mol^{-1} 5.52).

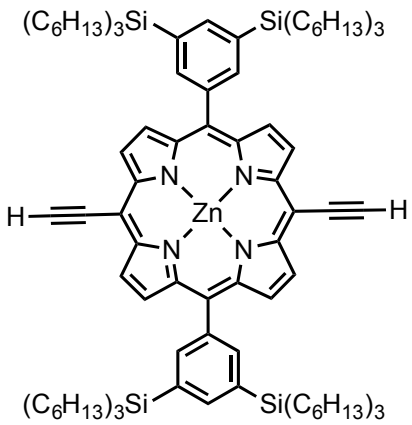

FIG. SI2: Chemical structure of the porphyrin molecule without anchor groups used for control experiments

D. Device Fabrication

The molecular devices were fabricated on a heavily doped silicon chip with a 300 nm thick oxide which also serves as a back gate to modulate charge transport through the junction. The graphene electrodes were fabricated based on the method of feedback-controlled electroburning as described in[4]. We use feedback-controlled electroburning to form nanometre-sized gaps in pre-patterned CVD-grown single-layer graphene ribbons. By this technique we can fabricate large numbers of almost identical single-molecule junctions. CVD-grown single-layer graphene is transferred onto a Si/SiO_2 chip that is pre-patterned with gold electrodes. Graphene is then patterned into a bowtie-shaped geometry by exposing a negative resist using e-beam lithography, followed by oxygen plasma etching. The bowtie-shaped geometry produces the highest current density in the centre of the device, resulting in the formation of the desired nano-gaps there. The feedback-controlled electroburning is performed in air at room temperature using an automated probe-station. This allows fabricating ca 500 devices in 48 hours on a single 1×1 cm^2 chip. The source-drain voltage is increased, while the current is monitored with a 200 μs sampling rate. When the feedback condition (i.e. a ΔI_{set} drop of the current within the past 15 mV) is met, the voltage is ramped back to zero. After each burning cycle the resistance between the gate and source and drain terminals is measured and the process is repeated until the low-bias resistance exceeds R_{set}. The samples were then immersed in a 10 μM chloroform solution containing the molecules for 30 mins. Devices were then wirebonded to our sample puck and transferred to our dilution fridge with a base temperature of 20 mK. All electrical measurements were performed using low noise, battery operated electronics, while the gate potential was modulated with a Keithley 2400 sourcemeter. For room temperature measurements, the devices were measured at a pressure of 4.3×10^{-3} mbar. It is necessary to measure the devices at low pressure as they are sensitive to the adsorption of ambient molecules.

II. TRANSPORT SPECTROSCOPY

A. Sequential electron tunneling

p	index of the molecular orbital state
E_p	single-electron molecular orbital energy
HOMO	highest occupied molecular orbital
LUMO	lowest unoccupied molecular orbital
Δ_{HL}	HOMO–LUMO gap
N	electron occupation of the molecule
U	total energy of the N-electron molecular state
GS	N-electron molecular ground state
ES	N-particle electron excited state
μ	electrochemical potential of the molecule
$\mu_{S(D)}$	electrochemical potential of the source(drain) electrode
E_F	Fermi level of the leads
E_{add}	addition energy
E_C	charging energy
δE	energy spacing between two discrete energy levels

In metals, the electrons are delocalised over collective states and described by band theory, which derives the electronic band structure through the quantum mechanical wavefunctions for electrons in large, periodic lattice of atoms or molecules. The dimensions of the metal can be reduced to a size such that quantization of the energy spectrum occurs, i.e. a set of discrete energy levels. Such a system is known as a quantum dot (QD). When a molecule is inserted between electrodes, the system produced is such that two electronic reservoirs characterized by filled energy bands are coupled with a system with discrete and quantized energy levels. Molecules can thus be compared to QDs, and much of the physics involved can be applied to both. The main difference between a molecule and QD is that the energy level spacing is intrinsic to the type of molecules, and depends on its molecular structure or conformation; in QDs, the level spacing is largely dependent on the material and geometry.

In a QD the number of electrons or holes can be controlled[5]. Current and voltage probes attached to these dots allow for the measurement of their electronic properties. In addition, the capacitance coupling of the dot to gate electrodes enables the tuning of the local electrostatic potential of the dot with respect to the reservoirs. In a molecule, this is akin to shifting the molecular levels with respect to the Fermi level E_F of the electrodes. How much the orbital levels E_n can be shifted by the potential applied to the gate electrode is quantified by the gate coupling parameter β. This should be as large as possible in order to access as wide a range of molecular energy levels as possible. This parameter is determined by the geometry and material of the system. Bulky Au electrodes can reduce the gate coupling substantially due to screening. In addition, the breakdown voltage of the gate oxide is also an important parameter to consider as it determines the maximum range of energy levels that can be probed. The two most frequently used gate materials are heavily doped silicon substrates with thermally grown silicon oxide on top and aluminum strips with a native oxide of a few nanometers. In aluminum gates with a 3 nm thick oxide, the gate coupling is 0.1[6], with a typical breakdown voltage of 4 V. In silicon devices with a 250 nm thick oxide layer, the gate coupling is $\sim 10^{-3}$, with a breakdown voltage of 100 V. This translates to a range of about $\pm$ 0.4 eV and $\pm$ 0.1 eV over which the potential on the molecule can be varied for aluminum and silicon gates respectively.

The molecular-lead coupling Γ_S, Γ_D, describes the overlap between the molecular wavefunction with that of the conduction electrons of the leads, and is also related to the tunneling rates between the each lead and the molecular level. The current through the SET can be written as a function of Γ_S and Γ_D (See section 3.2). The total coupling, $\Gamma = \Gamma_S + \Gamma_D$, is a measure of the resulting lifetime broadening of the molecular levels. Depending on the the value of Γ, three main regimes can be distinguished: (1) strong coupling, (2) weak coupling or (3) intermediate coupling. In the strong coupling regime ($\Gamma \gg E_C, \delta E$), the molecular states are mixed strongly with the wavefunction of the electrode, resulting in small barriers between the molecule and electrode. In the weak coupling regime ($\Gamma \ll E_C, \delta E$), the molecular states are well separated from the electrodes and the barriers are high. In the intermediate state, which is a mixture of the weak and strong coupling, the molecular and electrode wavefunctions are partially mixed. The molecular identity is retained; however, due to the lowered barrier, it can still be accessed by electrons from the electrodes. The value of Γ therefore determines the regime the system falls under. We shall focus on the regime most relevant to our single-molecule devices: weak coupling.

The electronic properties of weakly coupled systems are dominated by Coulomb interactions and spatial confinement. Charge transport in this regime can be conveniently described with the constant interaction model, which is based on two assumptions. (1) A single constant capacitance C, can be used to parameterize the Coulomb interactions between electrons in the molecule and between electrons in the molecule and the environment. C is equal to the sum of the capacitance between dot and source C_s,

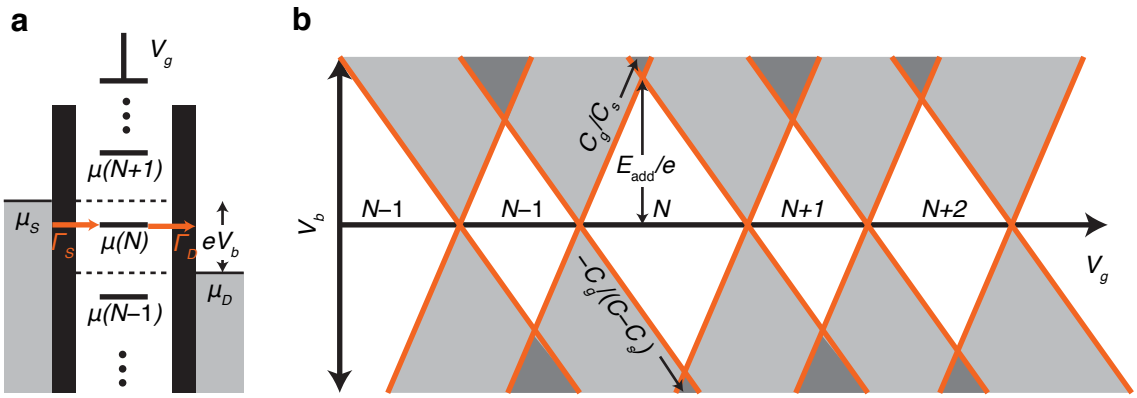

FIG. SI3: **Single-electron transport. (a)** Schematic of the electrochemical potential levels for different N. A potential V_b is applied acoss the electrodes, while a gate potential V_g tunes the chemical potential levels. $\Gamma_{S(D)}$ are the tunnel rates for the source (drain) electrode. **(b)** Schematic of a charge stability diagram for a molecule weakly coupled to source and drain electrodes defined by a chemical potential μ_S and μ_D. Light shaded regions correspond to single-electron transport through the molecule while white regions indicate Coulomb blockade. The dark shaded regions correspond to two-electron transport. Within the Coulomb blockade regions, the number of electrons N remains fixed. The slopes of the Coulomb diamond edges give information regarding the capacitances of the system. The addition energy E_{add} and the gate coupling $\alpha = C_g/C$ can be extracted from the height and width of the Coulomb diamonds.

drain C_d and gate C_g. (2) The single particle energies are independent of the Coulomb interactions and are therefore independent of the number of electrons.

We consider a molecule that is weakly coupled via tunnel barriers to two reservoirs. The molecule has single-electron molecular orbital energy levels at E_p ($p = 1, 2, 3, \ldots$) labeled in ascending order. Each level contains either one or zero electrons. Spin degeneracy is accounted for by counting each level twice, and other orbital degeneracies can be included similarly. The number of electrons N occupying the molecule can only take an integer value which defines the redox or charge state of the molecule. In the N-electron molecular ground state GS(N) the molecular orbital energy levels are occupied with N electrons in ascending order starting from $p = 1$. All other orbital configurations are N-electron excited states ES(N). We define the highest occupied molecular orbital (HOMO) energy level and lowest unoccupied molecular orbital (LUMO) energy level as the highest occupied and lowest unoccupied levels in the N-electron ground state. The energy difference between these levels is defined as the HOMO–LUMO gap Δ_{HL}. The first N-electron excited state is the orbital configuration in which one electron is promoted from the HOMO energy level to the LUMO energy level. The electrochemical potential of the molecule μ is defined as the difference between the total energy of the system with and without an additional electron during transitions between the states $|a>$ and $|b>$.

$$\mu_{a \leftrightarrow b} \equiv U_b(N) - U_a(N-1) \tag{1}$$

The available states for transport are thus denoted by μ. Figure 3a illustrates the electrochemical potential level schematic for a molecule weakly coupled to source and drain electrodes. For transistions between successive ground states, i.e. the energy required to add an extra electron, is referred to as the addition energy E_{add},

$$E_{\text{add}} = \mu(N) - \mu(N-1) = E_C + \delta E \tag{2}$$

where $E_C = e^2/2C$ is the charging energy due to Coulomb interactions and δE is the energy spacing between two discrete energy levels, which is zero for electrons added to the same spin degenerate level. Electron transport through the molecule depends on the alignment of the electrochemical potentials of the molecule with those of the source and drain. An energy window, also known as the bias window, $\mu_S - \mu_D = -eV_{SD}$, opens up when the bias V_{SD} is applied between the source and drain. In this case, the drain is connected to ground. Within this window, the electrons states in one reservoir are filled while the other is empty. Any chemical potential level involving the current state within the molecule that falls within this bias window results in sequential tunneling, i.e. electrons tunneling from filled reservoir onto the molecule, and off to the empty reservoir.

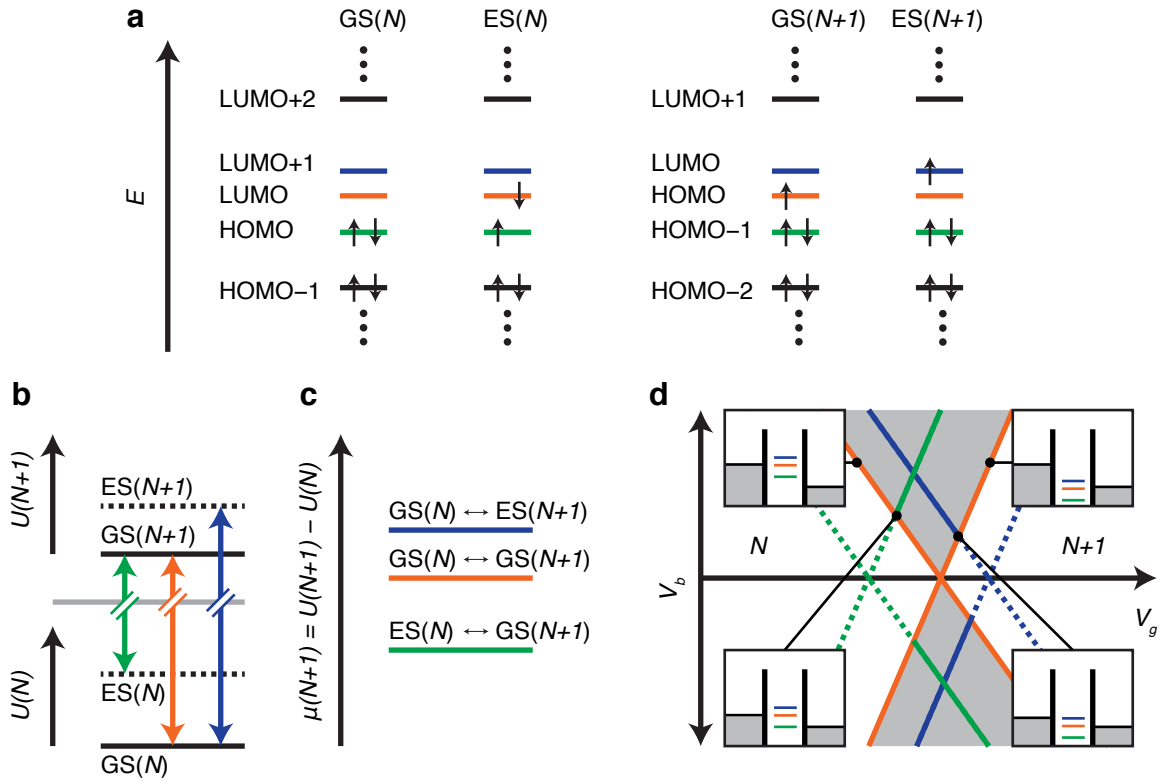

FIG. SI4: **Excited state spectroscopy. (a)** Energy level diagram of the ground states and excited states of the redox states N and $N+1$. The arrows indicate the spins of the electrons. **(b)** Energy level diagram for N electrons $U(N)$ and $N+1$ electrons $U(N+1)$. The relevant transitions are indicated by the coloured arrows. **(c)** The chemical potential ladder indicating the different transitions. **(d)** Schematic of a charge stability diagram indicating the different ground and excited state transitions. The insets indicate the corresponding alignment of the electrochemical potentials and the Fermi levels.

B. Excited state spectroscopy

In the low bias regime in equilibrium, transport can only occur when a transition between successive ground states falls within the bias window, i.e., $\mu_S \geq \mu(N) \geq \mu_D$ for at least one N. If no such transition can occur, transport is blocked through the molecule and the molecule is in Coulomb blockade (CB). This is illustrated in Figure 3b, where slopes separate regions of high conductance (single-electron tunneling (SET)) from diamond shaped regions (Coulomb diamonds) with almost zero conductance due to CB. Within the Coulomb diamonds, the number of electrons N is fixed. The gate voltage allows the tuning of μ and thus allows the number of electrons to be controlled. Between consecutive Coulomb diamonds, the charge on the molecule increases (decreases) by one as we go to more positive (negative) gate voltages. However, the absolute charge state of the molecule is difficult to determine as the neutral charge state of the molecule may not correspond to zero bias and gate due to partial charging of the molecule or background charges from electron traps that affect the dielectric environment of the system.

In the high bias regime, i.e., when the bias window is increased such that a transition involving an excited state also falls within, the number of paths that electrons can tunnel increase. This shows up as lines running parallel to the diamond edges within the SET regime. The energy δE can be read off as the distance from the zero-bias axis to the intersection point of the lines with diamond edges. E_{add} can be read off as the height of the Coulomb diamond along the bias axis. From Eqn. (1), the electrochemical potentials, μ, can be calculated for relevant transitions. For example, the transitions for two successive ground and excited states are considered in Figure 4. The excited states ES(N) and ES($N+1$) are separated from the ground states GS(N) and GS($N+1$) by $\delta E(N)$ and $\delta E(N+1)$ respectively. Information on the capacitances of the system can be extracted from the Coulomb diamond edges. The positive slope is $= C_G/(C - C_S)$ and the negative slope is $= -C_G/C$. The gate coupling $\alpha = C_G/C$ can thus be determined from the charge stability diagram.

For transitions terminating at the N-electron CB region, the transition necessarily involves an N-electron excited state and this result is true for any N. If N=0, no lines terminate at the CB region since there are no excited states for N=0. For transitions between two excited states, the line terminates at the region where the energy level spacing is larger. If $\delta E(N+1) > \delta E(N)$,

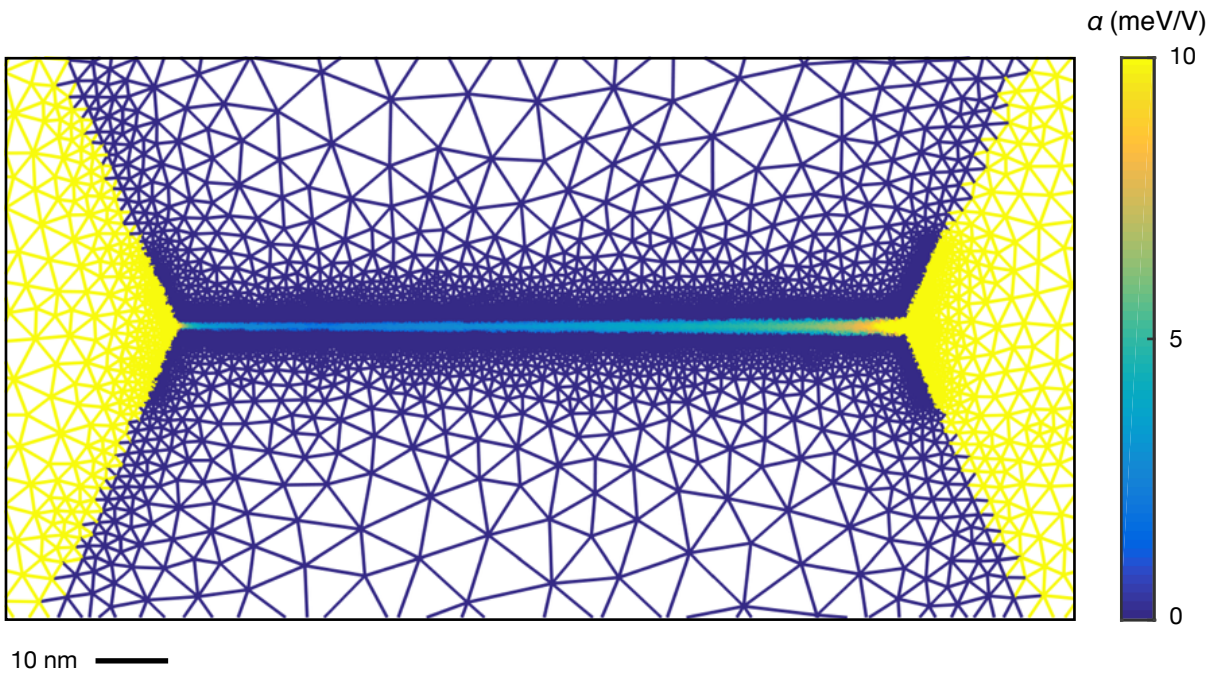

FIG. SI5: **Finite element model of the electrostatic gate coupling** The gate coupling α is calculated by deviding the potential in the source/drain plane by the voltage applied to the gate electrode. The gate electrode is seperated from the source/drain plane by 300 nm of SiO_2. The potential on the source and drain electrodes is fixed at zero. The gap between the source and drain electrodes ranges from 1 to 3 nm. The electrosctatic model was solved using COMSOL.

the line terminates at the N+1 CB region. The transition between excited states ES(N) $\leftrightarrow$ ES(N+1) is dependent on the relative magnitudes of the tunnel and relaxation rates. When the relaxation rate is larger than the tunnel rate Γ, the molecule is effectively constantly in its ground state and such a transition does not occur. In the opposite extreme, this transition participates in electron transport. Visibility of excited state transitions can thus provide an insight to the relative magnitudes of the tunnel and relaxation rates

C. Gate coupling

The gate coupling α strongly depends on the electrostatic screening of the gate electric field by the source and drain electrodes. We have estimated the gate coupling for a given electrode geometry by solving the Laplace equation using the COMSOL finite element software package. Figure SI5 shows the potential in the source/drain electrode plane that is induced by a voltage on the gate electrode, which is seperated from the source/drain electrodes by 300 nm of SiO_2. The gap between the source and drain electodes ranges is tapered from 3 to 1 nm, resulting in a variation in the potential in the gap. The magnitude and vaiation in gate coupling is consistent with our experimental observations.

D. Density of states in the graphene leads

Bias spectroscopy requires a source and drain of charge carriers in order to the states of the molecules. The density of states of the electrodes will strongly influence the behaviour of the single-molecule device as it determines the availabiltiy of charge carriers for tunneling. Gated graphene electrodes could pose a problem in this respect because of the fact that it has a zero carrier concentration at the charge neutrality point. However, gate modulation of the density of states in the leads does not inhibit our measurements for several reasons: i) the charge neutrality (Dirac) point V_D for CVD graphene on SiO_2 is typically far from zero gate voltage due to p-type doping. We find that $V_D > 40$ V for our devices (see Figure SI6); ii) at the charge neutrality point there is a residual carrier density due to defects in the graphene and the formation of charge puddles due to the underlying SiO_2; iii) it is well known that while the DOS vanishes at the charge neutrality point, the electrical conductivity does not (see eg Phys. Rev. B 75, 033405 (2007) and ref therein). This is because current is carried by evanescent states between metallic electrodes.

We can estimate the gate modulation of the electrochemical potential in the leads from the carrier concentration:

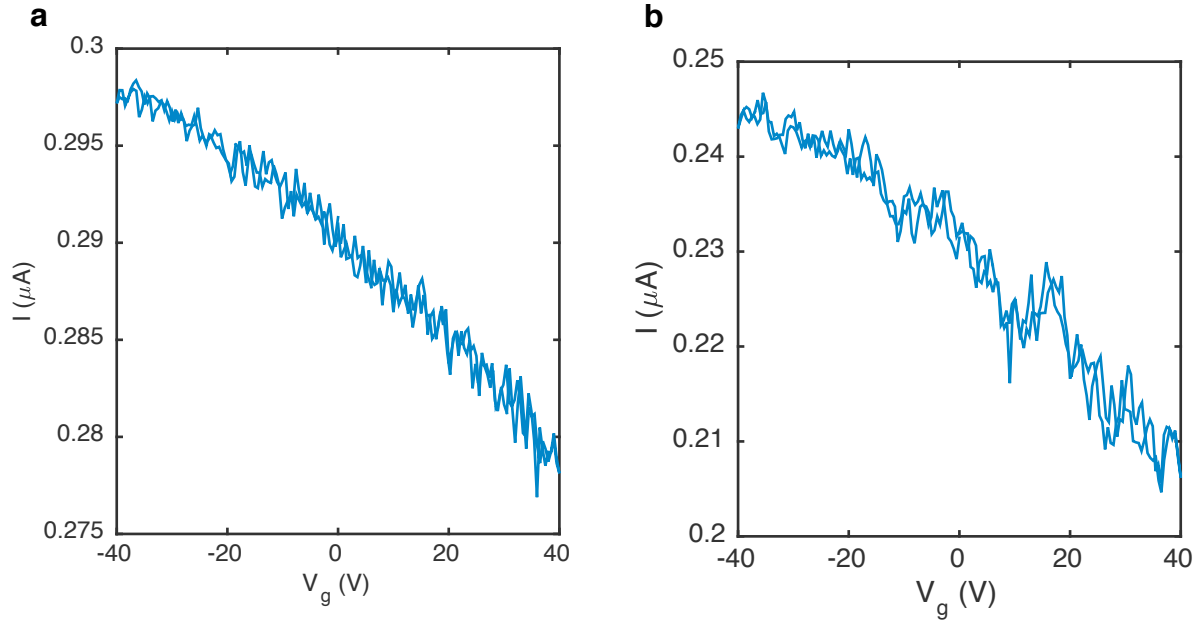

FIG. SI6: **Determination of the charge neutrality point** Graphene devices have a minimum conductance at the charge neutrality point ($V_G = V_D$). **a** Current as a function of gate voltage for a un-burned device. The conductance minimum is outside the gate range $V_D > 40$ V. Measured at a bias voltage $V_b = 5$ mV. **b** Current as a function of gate voltage after one burn cycle.

$$n = \sqrt{n_0^2 + C_G(V_G - V_D)}, \tag{3}$$

whre n_0 is the minimum sheet carrier concentration as determined by disorder and thermal excitation. The electrchemical potential in the leads is give by:

$$\mu_{L,R} = \hbar v_F \sqrt{n}, \tag{4}$$

where $v_F \sim 10^6$ m/s is the Fermi velocity in graphene. Assuming zero residual charge carriers and $V_D = 40$, we estimate the upper-bound of shift of the electrochemical potential over the -40 V to +40 V gate range to be < 0.3 eV.

E. Charge traps

Change in population of a nearby charge centre can give rise to sequential tunneling featers such as non-closing and overlapping Coulomb diamonds as sketched in Fig. SI7[7].

III. CALCULATIONS

A. DFT details

The xyz coordinates of the molecule and graphene electrodes were initially extracted with the Avogadro package. Given the initial coordinates, the optimized ground state geometry of the gas phase molecule as well as graphene-molecule-graphene device was self-consistently obtained using the SIESTA[8] implementation of density functional theory (DFT). SIESTA employs norm-conserving pseudo-potentials to account for the core electrons and linear combinations of atomic orbitals to construct the valence states. The generalized gradient approximation (GGA) of the exchange and correlation functional was used with

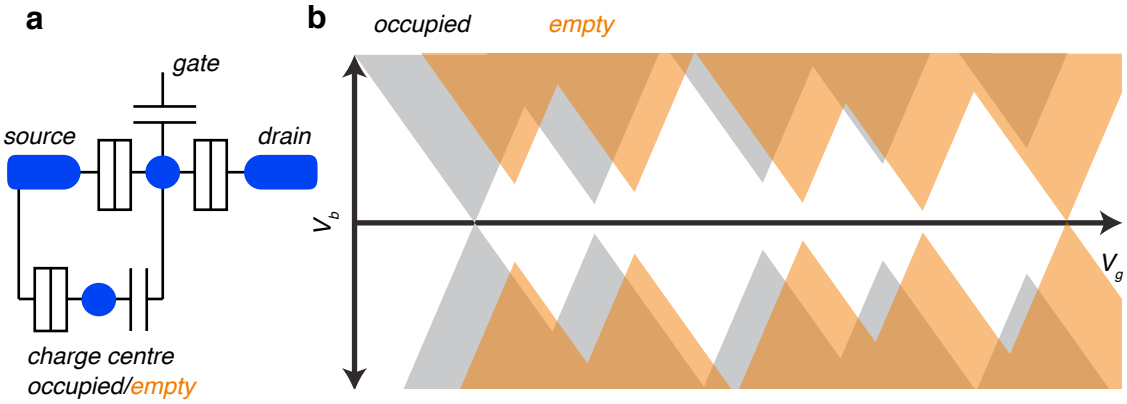

FIG. SI7: **Multiple charging events. a** circuit diagram of a single-molecule transistor with source, drain and gate. A nearby, capactively coupled, charge centre is sketched as a parasitic dot carrying no current. This charge centre can either be a oxide trap or a nearby molecule. The occupation of the charge centre changes the electrochemical potential of the molecule under investigation and shifts the Coulomb diamonds, as sketched in **b**. The overlap between the Coulomb diamonds for an occupied and an unoccupied charge centre result sequential tunneling features as observed in for example device 7 and 9.

the Perdew-Burke-Ernzerhof parameterization (PBE)[9] a double-ζ polarized (DZP) basis set, a real-space grid defined with an equivalent energy cut-off of 250 Ry. The geometry optimization was performed to the forces smaller than $40meV/\AA$. To find the HOMO-LUMO gap, the total energy of the ground state gas phase molecule was calculated for the neutral molecule as well as when the net-charge of the system is ± 1. The mean-field Hamiltonian (H) and overlap matrix (S) were obtained for the converged DFT calculation. The iso-surfaces of the calculated molecular orbital levels in the HOMO and LUMO states were visualized using the XCrySDen package[10].

B. Transport details

The mean-field Hamiltonian obtained from the converged DFT calculation is combined with our implementation of the non-equilibrium Green's function method (the GOLLUM[11]) to calculate the phase-coherent, elastic scattering properties of the system consisting of left (source) and right (drain) electrodes and the molecule. The transmission coefficient $T(E)$ for electrons of energy E (passing from the source to the drain) is calculated via the relation:

$$T(E) = Tr(\Gamma_D(E)G^R(E)\Gamma_S(E)G^{R\dagger}(E)) \tag{5}$$

In this expression, $\Gamma_{L,R}(E) = i(\sum_{L,R}(E) + \sum^{\dagger}_{L,R}(E))$ describe the level broadening due to the coupling between source (S) and drain (D) electrodes and the central scattering region, $\sum_{S,D}(E)$ are the retarded self-energies associated with this coupling and $G^R = (ES - H - \sum_S - \sum_D)^{-1}$ is the retarded Green's function, where H is the Hamiltonian and S is the overlap matrix. Using obtained transmission coefficient $T(E)$, the conductance could be calculated by Landauer formula $G = G_0 \int dET(E)(\partial f/\partial E)$ where $G_0 = 2e^2/h$ is the conductance quantum. Note that transmission coefficient $T(E_F) = G/G_0$ where temperature $T = 0K$. In addition, the current I through the device at voltage V could be calculated as:

$$I(V) = \frac{2e}{h}\int_{-\infty}^{+\infty} dET(E,V)[f_S(E+eV) - f_D(E)] \tag{6}$$

where $f(E) = (1+e^{(E-E_F/k_BT)})^{-1}$ is the Fermi-Dirac distribution function, T is the temperature and $k_B = 8.6\times10^{-5}eV/K$ is Boltzmanns constant.

For a gas phase system (without electrodes), the additional energy E_{add} is the energy difference between the N-electron ground state of the molecule and its N$\pm$1-electron ionized state[12]. However, in the presence of the graphene electrodes, due to the screening effect the additional energy would be significantly different from the gas phase system[13]. For the gas phase system, this could be defined as the difference between the ionization potential (IP) and electron affinity (EA) $E_{\text{add}} = IP - EA = [E(N-1) - E(N)] - [E(N) - E(N+1)]$. To obtain the E_{add} of the molecule, we use density functional theory to calculate

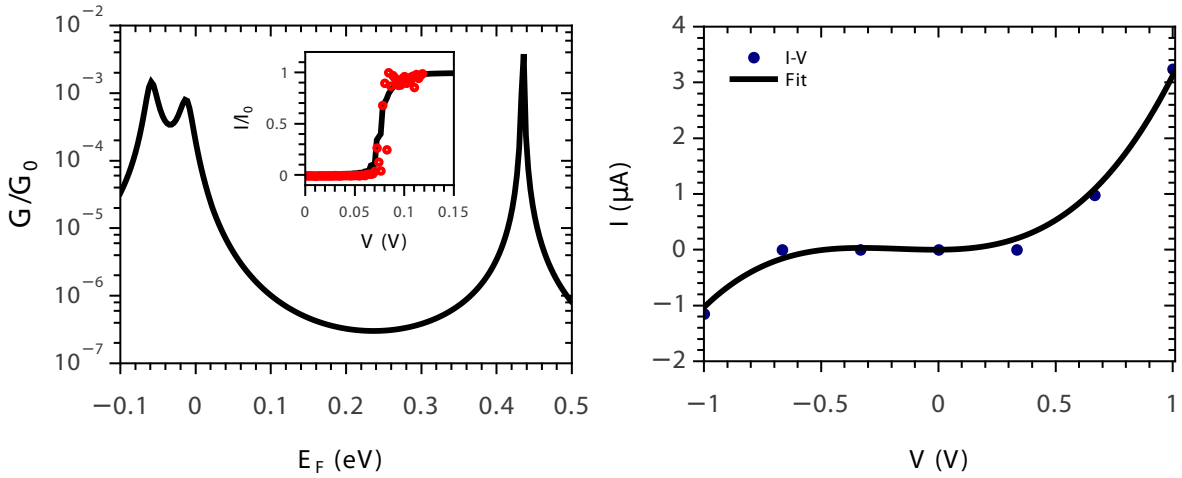

FIG. SI8: **Transport properties of the graphene-molecule-graphene transistor. a,** Conductance (G/G_0) versus Fermi energy (E_F) (inset: Experimental (red dots) and theoretical (solid lines) room temperature equilibrium $I-V$, **b,** Calculated non-equilibrium $I-V$ characteristic of the device (dark blue dots) and its fit (solid line).

the total energy of the neutral ground state and excited states of gas phase molecule (see methods). The IP and EA are calculated as 5.2 eV and 1.36 eV respectively which yields E_{add} = 3.84 eV. This is an order of magnitude higher than the measured E_{add}. This is a result of the re-normalization of the molecular charge energy due to the interaction with image charges and coupling to vibrations in the presence of the graphene electrodes. The image charges could be calculated either by some approximations or expensive self-consistent GW calculation which is practically applicable for small molecules. The best prediction based on GW method was obtained in small molecules where the predicted gap is two times the measured gap[14]. In most cases the approximated gap gives results that are very similar to those obtained with more expensive methods. The image charge could be approximately calculated as: $W = \frac{e^2 ln2}{8\pi\epsilon_0 a}$ where a = 3.2 Åis the distance between the surface of the graphene electrodes and the surface of the butterfly anchor groups[15]. This correction reduces the additional energy to 740 meV which is in close agreement with the experiment. To further study the orbital structure of the molecule, we have computed the molecular orbital for HOMO and LUMO states. Figure 1c in the main text shows the local density of states (LDOS) for the HOMO and LUMO levels in the gas phase molecule. The molecular orbitals are mostly localized in the zinc-porphyrin backbone for the LUMO level. In contrast for the HOMO, the molecular orbitals are not only localized in the zin-porphyrin backbone, but also in the butterfly anchor groups. Consequently, we expect HOMO dominated transport in this molecule. We investigated the phase-coherent, elastic scattering properties of the molecule bound to two left and right electrodes by $\pi-\pi$ interaction between the butterfly anchor groups and surface of the graphene electrodes. The geometry optimization performed by DFT to find the ground state relaxed structure in the presence of the graphene electrods is shown in Figure 1b in the main text. The average distance between the butterfly anchor groups and surface of the graphene electrodes was found to be 3.2 Å, where the butterfly anchor groups shows mixed AA and AB stacking with the graphene electrodes. Figure 5a shows the transmission coefficient ($T(E_F) = G/G_0$ in $T = 0K$ temperature) for the electrons of energy E passing from the source to the drain. The HOMO resonance was found to be close to the Fermi energy ($E_F = 0$) as expected from LDOS calculation. The spectral adjustment was performed to correct the Kohn-Sham HOMO-LUMO gap based on the experimental values[11]. The molecule shows fairly high conductance in the Fermi energy ($G/G_0 = 2\times10^{-4}$). The inset of Figure SI8 shows the measured (red dots) and calculated (solid lines) normalized zero bias IV in room temperature where the Fermi energy is in the middle of the HOMO-LUMO gap. To demonstrate the rectification properties of our graphene-molecule-graphene transistor, we have performed NEGF calculation to calculate voltage dependence transmission coefficients $T(E,V)$ and found the source drain current I versus bias voltage V as shown in Figure SI8. Although the molecule is symmetric, the device shows rectification properties due the asymmetry of the contacts. The butterfly anchor groups is not completely flat and its configuration on top of the graphene is different in two contacts (see Figure 1b in main text).

IV. MEASUREMENTS

A. Cryogenic Stability Diagrams

Device	E_{add} (eV)	α	V_{g0} (V)
1	0.44	7.4×10^{-3}	14
2	0.44	6.1×10^{-3}	25
3	0.35	6.5×10^{-3}	25
4	0.39	8.6×10^{-3}	15
5	0.38	7.7×10^{-3}	27
6	0.29	3.9×10^{-2}	0
7	0.39	8.5×10^{-3}	15
8	0.31	1.9×10^{-2}	12
9	0.34	1.6×10^{-2}	12
10	0.36	9.3×10^{-3}	22

The charge stability diagrams for all 10 devices shown in the main text are shown in Figure 6 and 7 without scaling and offseting the gate axis with α and V_{g0}. The corresponding current scale is shown for each diagram.

B. Room Temperature Stability Diagrams

Room temperature charge stability diagrams for device 2 (Figure SI11), 3 (Figure SI12) and 6 (Figure SI13) are shown. Notable differences can be observed between the measurements taken at room and cryogenic temperatures. There is substantially more noise due to thermal fluctuations. In addition, random switching events in the current can be observed even with low gate voltage, as compared to cryogenic measurements where only occasional switches were observed at large gate voltages. As the devices are fabricated on a heavily doped silicon substrate with a thermally grown oxide layer, this is possibly attributed to dopants and trapped charges in the vicinity that are more mobile at elevated temperatures. This leads to sudden changes in the electrostatic potential at the molecule which alters μ. The presence of these dopants and trapped charges modifies the dielectric environment and thus capacitances of the system, which is reflected in the changing slopes that define the Coulomb diamond edges. It is likely that the replacement of our thick gate oxide will lead to improved stability. Aluminum substrates with a native oxide of a few nanometers will greatly improve α, with α values ~ 100 times higher than silicon oxide, and will therefore negate the requirement for large applied gate voltages to access several redox states. Recently, hexagonal boron nitride has been proposed as an excellent substrate for graphene devices, with reported mobilities and carrier inhomogeneities that are almost an order of magnitude better than silicon oxide[16]. Its atomically smooth surface is relatively free of dangling bonds and charge traps and should substantially improve the stability of our devices.

V. SINGLE-ELECTRON LOGIC

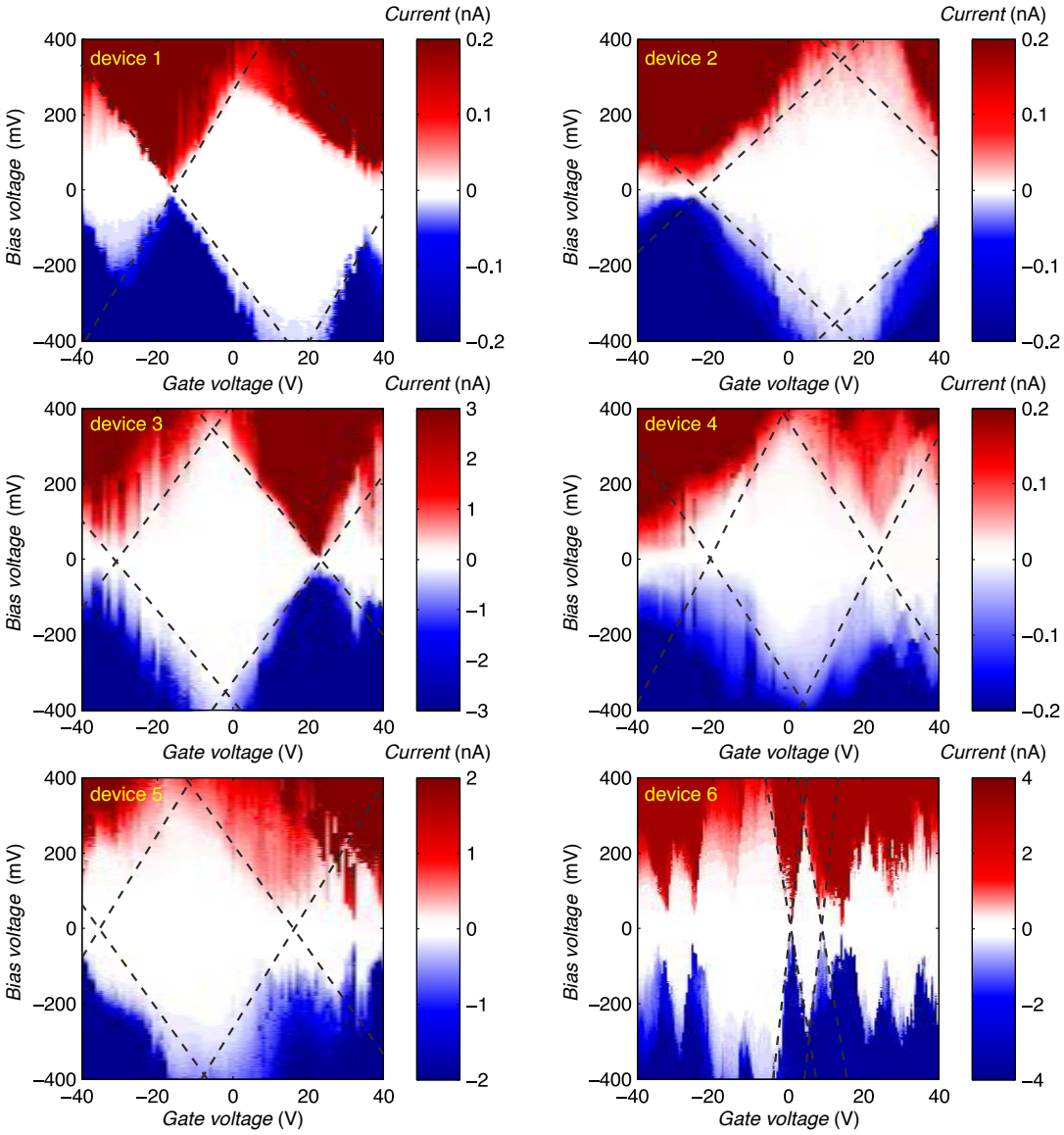

FIG. SI9: Charge stability diagrams (current as a function of bias and gate voltage) for devices 1 to 6.

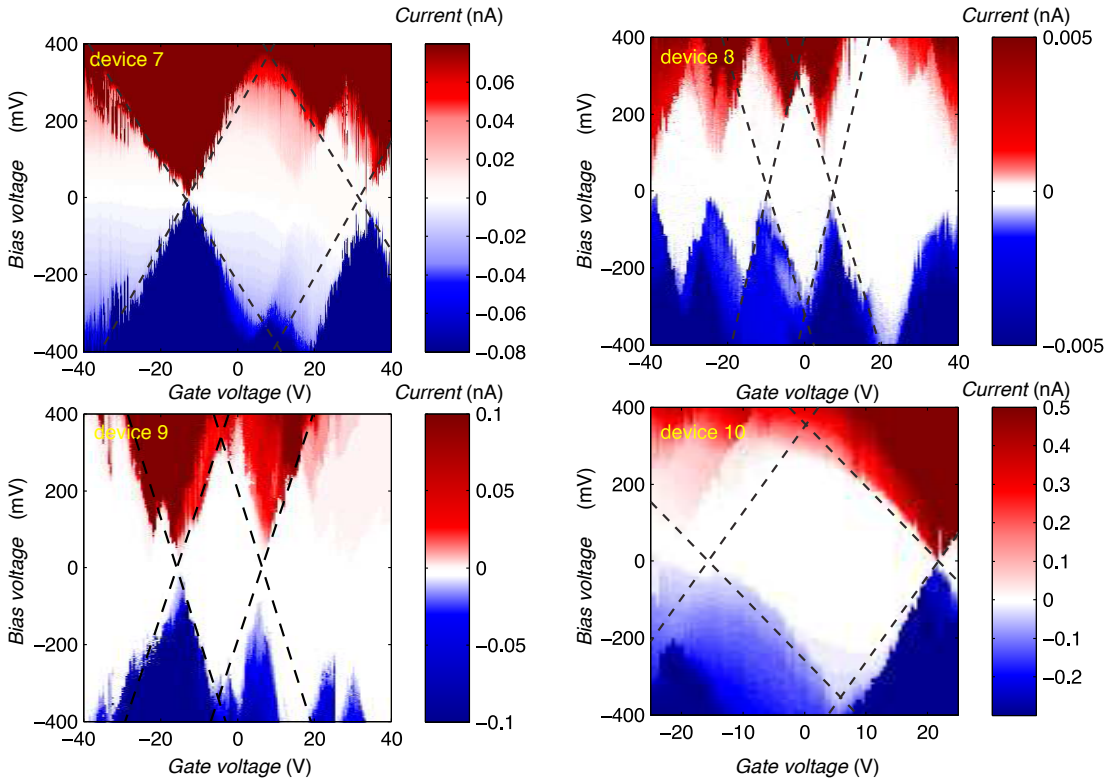

FIG. SI10: Charge stability diagrams (current as a function of bias and gate voltage) for devices 7 to 10.

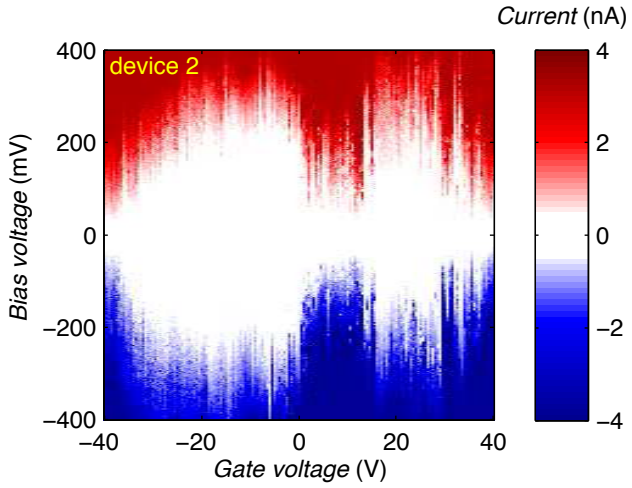

FIG. SI11: Room temperature charge stability diagram (current as a function of bias and gate voltage) of device 2

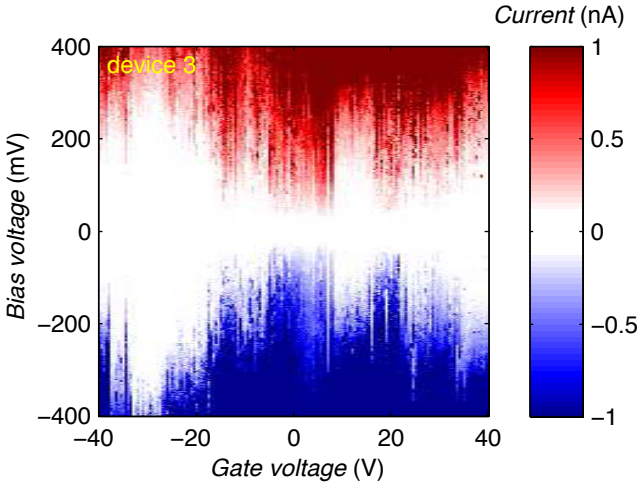

FIG. SI12: Room temperature charge stability diagram (current as a function of bias and gate voltage) of device 3

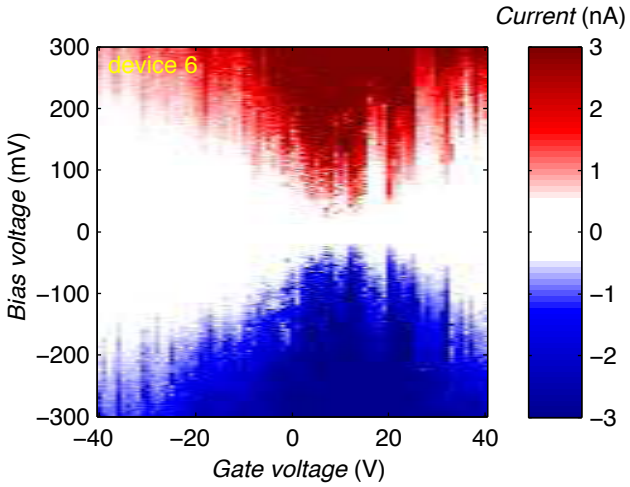

FIG. SI13: Room temperature charge stability diagram (current as a function of bias and gate voltage) of device 6

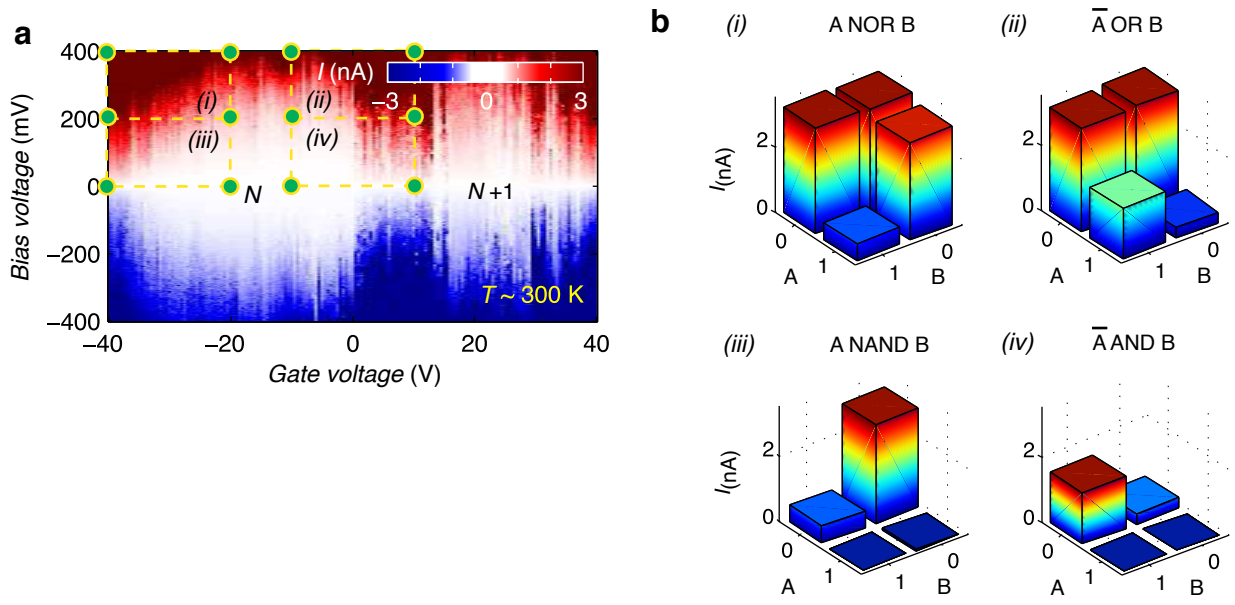

FIG. SI14: **Room temperature Coulomb blockade in a single-molecule transistor.** a Current stability diagram as a function of V_b and V_g measured at room temperature. **b** Four different logic operations can be performed at room temperature using the same device: A NOR B, $\overline{A}$ OR B ($\overline{A}$ denotes NOT A), A NAND B and $\overline{A}$ AND B. The logic inputs are taken as: (i) and (ii) $V_b = 400$ mV $\rightarrow A = 0$, $V_b = 200$ mV $\rightarrow A = 1$; (iii) and (iv) $V_b = 200$ mV $\rightarrow A = 0$, $V_b = 0$ mV $\rightarrow A = 1$; (i) and (iii) $V_g = -40$ V $\rightarrow B = 0$, $V_g = -20$ V $\rightarrow B = 1$; (ii) and (iv) $V_g = -10$ V $\rightarrow B = 0$, $V_g = 10$ V $\rightarrow B = 1$.

[1] Grozema, F. C., Houarner-Rassin, C., Prins, P., Siebbeles, L. D. A. & Anderson, H. L. Supramolecular Control of Charge Transport in Molecular Wires. *Journal of the American Chemical Society* **129**, 13370–13371 (2007).

[2] Dutton, J. K., Knox, J. H., Radisson, X., Ritchie, H. J. & Ramage, R. Synthesis of 17H-tetrabenzo[a,c,g,i]fluorene derivatives as chiral selectors for enantiomeric separation by HPLC on porous graphitised carbon. *Journal of the Chemical Society, Perkin Transactions 1* 2581 (1995).

[3] Assali, M. *et al.* Improved non-covalent biofunctionalization of multi-walled carbon nanotubes using carbohydrate amphiphiles with a butterfly-like polyaromatic tail. *Nano Research* **3**, 764–778 (2010).

[4] Lau, C. S., Mol, J. A., Warner, J. H. & Briggs, G. A. D. Nanoscale control of graphene electrodes. *Physical Chemistry Chemical Physics* 20398–20401 (2014).

[5] Hanson, R., Petta, J. R., Tarucha, S. & Vandersypen, L. M. K. Spins in few-electron quantum dots. *Reviews of Modern Physics* **79**, 1217–1265 (2007).

[6] Osorio, E. A., Bjørnholm, T., Lehn, J.-M., Ruben, M. & van der Zant, H. S. J. Single-molecule transport in three-terminal devices. *Journal of Physics: Condensed Matter* **20**, 374121 (2008).

[7] Escott, C. C., Zwanenburg, F. A. & Morello, A. Resonant tunnelling features in quantum dots. *Nanotechnology* **21**, 274018 (2010).

[8] Soler, J. M. *et al.* The SIESTA method for ab initioorder- Nmaterials simulation. *Journal of Physics: Condensed Matter* **14**, 2745–2779 (2002).

[9] Perdew, J. P., Burke, K. & Ernzerhof, M. Generalized Gradient Approximation Made Simple. *Physical Review Letters* **77**, 3865–3868 (1996).

[10] Kokalj, A. Computer graphics and graphical user interfaces as tools in simulations of matter at the atomic scale. *Proceedings of the Symposium on Software Development for Process and Materials Design* **28**, 155–168 (2003).

[11] Ferrer, J. *et al.* GOLLUM: a next-generation simulation tool for electron, thermal and spin transport. *New Journal of Physics* **16**, 093029 (2014).

[12] Zhan, C.-G., Nichols, J. A. & Dixon, D. A. Ionization Potential, Electron Affinity, Electronegativity, Hardness, and Electron Excitation Energy: Molecular Properties from Density Functional Theory Orbital Energies. *The Journal of Physical Chemistry A* **107**, 4184–4195 (2003).

[13] Perrin, M. L. *et al.* Large tunable image-charge effects in single-molecule junctions. *Nature Nanotechnology* **8**, 282–287 (2013).

[14] Strange, M., Rostgaard, C., Häkkinen, H. & Thygesen, K. S. Self-consistent GW calculations of electronic transport in thiol- and amine-linked molecular junctions. *Physical Review B* **83**, 115108 (2011).

[15] García-Suárez, V. M. & Lambert, C. J. First-principles scheme for spectral adjustment in nanoscale transport. *New Journal of Physics* **13**, 053026 (2011).

[16] Dean, C. R. *et al.* Boron nitride substrates for high-quality graphene electronics. *Nature Nanotechnology* **5**, 722–726 (2010).